SCIENCE CHINA
Chemistry

•ARTICLES•

April 2024 Vol.67 No.4: 1289–1299
https://doi.org/10.1007/s11426-024-1972-7

A nitric oxide-triggered hydrolysis reaction to construct controlled self-assemblies with complex topologies

Wenzhuo Chen[1,2], Yuping Tang[1], Shuai Chen[3], Zipei Chen[2], Jia He[2], Hongbin Huo[2], Juan Zhang[2], Jiajia Li[1], Fei Yan[1] & Wei Tian[2*]

[1]*Laboratory of Shaanxi Administration of Traditional Chinese Medicine for TCM Compatibility, Shaanxi Key Laboratory of Chinese Medicine Fundamentals and New Drugs Research, College of Pharmacy, Shaanxi University of Chinese Medicine, Xianyang 712046, China;*
[2]*Shaanxi Key Laboratory of Macromolecular Science and Technology, Xi'an Key Laboratory of Hybrid Luminescent Materials and Photonic Device, MOE Key Laboratory of Material Physics and Chemistry under Extraordinary Conditions, School of Chemistry and Chemical Engineering, Northwestern Polytechnical University, Xi'an 710072, China;*
[3]*Department of Polymeric Materials, School of Materials Science and Engineering, Tongji University, Shanghai 201804, China*

Received January 16, 2024; accepted February 17, 2024; published online March 18, 2024

Hydrolysis reactions are capable of directing the non-equilibrium assembly of biomolecular scaffolds to realize sophisticated structures and functions in natural systems. However, utilizing the proper hydrolysis reactions to construct controlled assemblies with complex topologies is still an arduous challenge in artificial systems and needs to be addressed. Herein, we report a nitric oxide (NO)-triggered slow hydrolysis strategy for the controlled construction of biomimetic supramolecular toroids (STs), thus realizing their visualization of intermediate structures and regulation of geometry parameters. This presented protocol harnesses hydrolysis reactions to control of non-equilibrium self-assembly processes for the construction of self-assemblies with complex topologies successfully, which sheds light on how the hydrolysis reaction rate can modulate the kinetic pathway of assembly, thus realizing the artificial establishment of bio-inspired hierarchical structures.

supramolecular toroids, controlled self-assembly, nitic oxide-triggered hydrolysis, pathway regulation

Citation: Chen W, Tang Y, Chen S, Chen Z, He J, Huo H, Zhang J, Li J, Yan F, Tian W. A nitric oxide-triggered hydrolysis reaction to construct controlled self-assemblies with complex topologies. *Sci China Chem*, 2024, 67: 1289–1299, https://doi.org/10.1007/s11426-024-1972-7

1 Introduction

Hydrolysis reactions are capable of splitting substrate into two fragments which are rich in hydrogen bond (H-bond) groups, offering distinct insight into the regulation of supramolecular self-assembly, owing to tuning the rate of H-bond driven molecular rearrangement [1]. In a natural system, hydrolysis reactions are well-known for their ability to regulate biological activities *via* directing the non-equilibrium assembly of biomolecular scaffolds to realize sophisticated structures and functions. For instance, microtubules as highly dynamic and dissipative structures, which play an essential role in cell division, are self-assembled and disassembled by GTP hydrolysis to exert biological functions under non-equilibrium states. Thus, new strategies capitalized on hydrolysis reactions are promising to yield complex non-equilibrium nanostructures in artificial systems.

Despite these advances, the hydrolysis reactions controlled self-assembly are most commonly confined to inorganic systems, such as three-dimensional (3D) dendritic TiO_2, mesoporous silica fibers, and TiO_2-filled mesoporous metal-organic framework (MOF) [2]. Besides, a few examples concerning organic species are found in dissipative self-

*Corresponding author (email: happytw_3000@nwpu.edu.cn)

assembly system driven by chemical fuels, which cannot maintain the relatively stable structures after removal of the influx of energy [3]. Notwithstanding, the hydrolysis reactions controlled non-dissipative self-assembly systems including both thermodynamic equilibrium state and kinetic non-equilibrium with relatively stable morphologies have been rare reported for extensive functionality and application. In addition, it remains a challenge to develop assemblies with control of geometry parameters and visualization of dynamic formation pathways through hydrolysis reactions driven self-assembly strategy. Therefore, harnessing hydrolysis reactions to regulate non-dissipative self-assembly processes can offer intriguing approach towards complex self-assembled structures and functional materials, as well as contributions to the understanding of the assembly mechanism.

Based on the background of the aforementioned hydrolysis induced self-assembly, as well as our research group's understanding in controllable self-assembly [4], here we envisage to launch a hydrolysis reaction controlled supramolecular system to retard the rate of self-assembly and modulate its pathway, thus realizing the efficient construction, formation process visualization, and structural parameter regulation of the self-assemblies with complex topologies. Specifically, the host-guest interaction based primary supramolecular micelles (PSMs) are first formed similar to other system [5], which can be slowly hydrolyzed under the biological signaling molecule nitric oxide (NO) [6,7] (Scheme 1A). As a result, the unique biomimetic supramolecular toroids (STs) with distinct topologies of ring shape and controllable geometry parameters including height (R_h), width (R_w), and diameter (R_d) could be obtained after the hydrolysis reaction at a time scale of hours, based on a nucleation-elongation mechanism. Further investigations on the self-assembly mechanism of STs show that the slow hydrolysis is of vital importance throughout the two-stage formation process of STs. At the first stage, the slow hydrolysis leads to the transformation from PSMs to wormlike micelles (WMs) by disordered entropy-driven nucleation, H-bond-driven growth and fusion process (Scheme 1A–C). In the latter stage, it contributes to a semi-rigid structure to subtle and synergistic balance the interfacial energy and bending energy for the curvature and closure of long WMs to form the intact STs (Scheme 1C–E). Comparatively, 2D nanosheets (NS) in thermodynamic equilibrium state were obtained by both simulated NO-triggered fast hydrolysis pathway and heating-slow cooling process, further suggesting a non-equilibrium state (kinetical trap) of the resulting STs (Scheme 1F).

2 Experimental

^{1}H nuclear magnetic resonance (NMR) spectra and ^{13}C NMR spectra were performed at 298 K on Bruker 400 MHz spectrometer or Bruker 500 MHz spectrometer (Germany). High-resolution mass spectra (HR-MS) were recorded with a Bruker Esquire 3000 plus mass spectrometer instrument

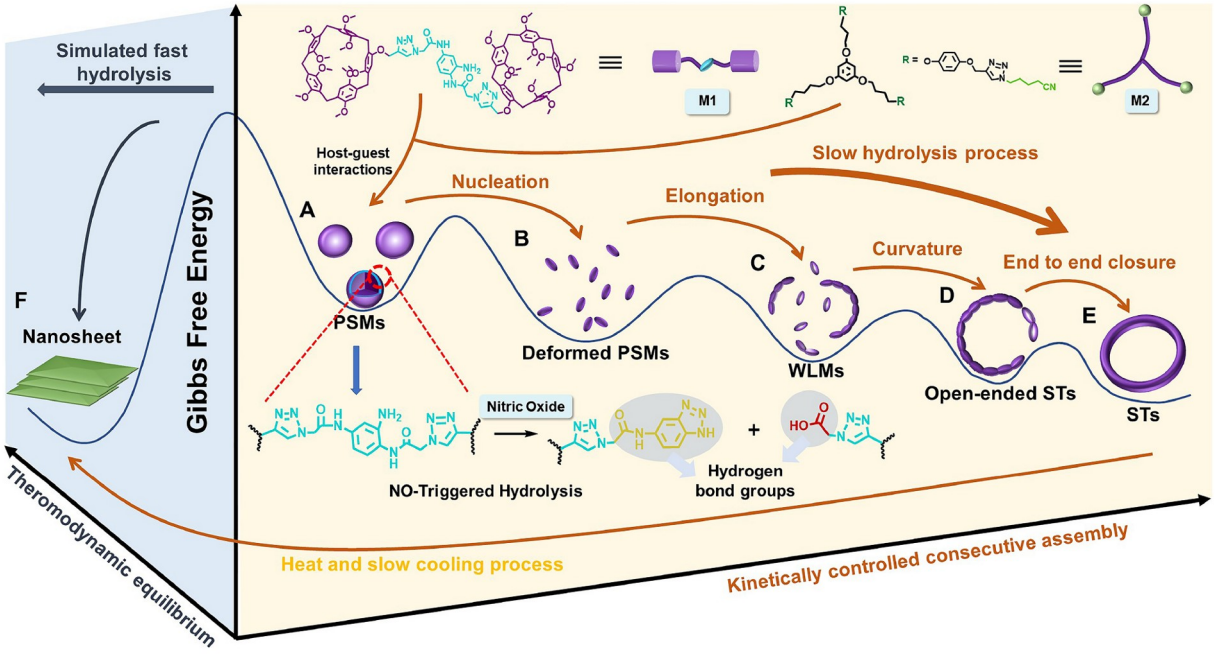

Scheme 1 Schematic representation of visual formation process of self-assemblies with complex topologies through nitric oxide triggered hydrolysis reaction. (A, B) NO-triggered slow hydrolysis leads to the deformation of PSMs with a nucleation process. (B, C) H-bonds driven elongation process to induce the formation of WMs. (C, D) WMs coil to open-ended STs under cooperative coalescence and curvature. (D, E) Open-ended STs evolve to intact STs by end to end closure. (F) 2D NS formation *via* simulated fast hydrolysis reaction (color online).

(Germany). The sample for transmission electron microscopy (TEM) and high-angle annular dark field-scanning TEM (HAADF-STEM) was examined by an FEI Talos F200X instrument (USA). Atomic force microscopy (AFM) was recorded at a tapping mode under ambient condition by using a Bruker Dimension FastScan and Dimension Icon instrument (Germany). Wide-angle X-ray scattering (WAXS) patterns were measured with SAXSpoint 2.0 small-angle X-ray scattering instruments. Infrared spectra data were obtained on a Bruker Tensor II infrared spectrometer (Germany). Ultraviolet-visible (UV-vis) spectra experiment was carried out on Shimadzu UV-2550 spectrophotometer (Japan). Hydrodynamic diameter was measured by using a Zeta sizer Nano ZS90 (UK) before sample was filtered.

2.1 General procedures of STs formation

In a typical preparation procedure, a fixed 3:2 complexation stoichiometry of M1 (5.21 mg, 3 μM) and M2 (2.23 mg, 2 μM) monomers were first dissolved in 100 mL chloroform with a trace amount of water and dimethylsulfoxide (DMSO, 0.5 mL, respectively), and then NO gas was charged. After 24 h for complete reaction, STs were obtained finally.

2.2 Measurement of size parameters of STs by AFM

According to the preparation illustration of STs specimens, STs in the concentration range from 30–70 μM were prepared three times independently for the AFM test. More than 100 toroids per sample were collect for the statistics. As shown in Scheme 2, the average size parameters including cross-sectional diameter (R_d), width (R_w), and height (R_h) of toroids were measured to estimate the relationship between the concentration and size parameters. Note that the size parameters are measured with a software ImageJ (National Institutes of Health, USA, version 1.48). The statistics and nonlinear fitting are conducted by originpro software (version 2021b). The error bars represent the estimated standard deviations, $\sigma = \sqrt{\left[\sum_1^i (N_i - \overline{N})^2 / i\right]}$, where i is the survey times (i = 3) and distribution frequency N is defined as the ratio of various morphologies by measuring a fixed field of view of AFM (1 mm^2).

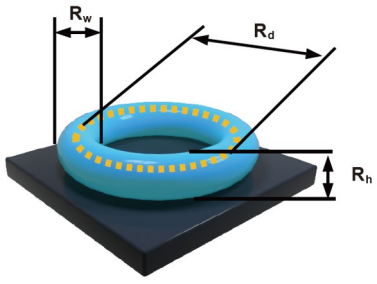

Scheme 2 Average size parameters including cross-sectional diameter (R_d), width (R_w), and height (R_h) of toroids (color online).

2.3 The basic principles and methods of calculation

The formation and dissociation of the supramolecular self-assemblies were also investigated *via* molecular dynamics (MD) simulations. MD simulations adopt Newton's equations of motion for the calculation of all-atom trajectories, acquiring thermo-dynamic properties of molecular systems comprising different molecular and structural models. The structural changes and formation of new interactions lead to the change in overall energy under simulated forces. As the structure becomes more stable, the overall energy decreases. All the simulations were carried out by the software of Materials Studio 2017. Models of molecules were created and optimized before incorporating into a "cell" where molecules interact with each other under certain operation parameters. To simplify the calculations and also to maintain the integrity of the structure, the supramolecular interlocking bond of P5 and alkylated cyano group was replaced by a chemical bond and the size of molecules were cut down to allow efficient calculations. The forcefield was COMPASS (version 2.8). The dynamics simulations were carried out with an ensemble of NVT where temperature was set to 298 K. The value of energy was obtained by the task of energy within the module of Forcite.

3 Results and discussion

3.1 NO-triggered slow hydrolysis reaction to construct STs

Two elaborately designed monomers termed M1 and M2 were first synthesized. One dumbbell-shaped M1 bearing a NO-reactive amide-functionalized *o*-phenylenediamine (APDA) linker and two pillar[5]arene (P5) host terminals, was obtained by the click reaction with high yield (84.2%, Scheme S1, Supporting Information online). The other M2 with *C*3 symmetry, which consists of three homotropic alkyl cyano binding sites as guests at each end of the molecule, was also synthesized by the click reaction (Scheme S2). Detailed synthetic routes and fully characterized results of both M1 and M2 are shown in Figures S1–S21 (Supporting Information online). ^{1}H NMR spectroscopy, 2D nuclear overhauser effect spectroscopy (2D NOESY) and UV-vis experiments were then performed to examine the strong host-guest interaction with a stoichiometry of 1:1 between alkylated cyano group in M2 and P5 unit of M1 in chloroform (for a detailed discussion see Figures S22–S25). Furthermore, the formed self-assemblies (also called PSMs) based on the host-guest and hydrophobic interactions between M1 and M2 are confirmed as well (for a detailed

discussion see Figure S26).

To clarify the NO-responsive hydrolytic behavior of PSMs, a kinetics protocol to appraise the hydrolysis process of M1 bearing APDA-linker in real time was conducted first by UV-vis spectrophotometry. M1 could react with NO accompanied by slow hydrolysis to form two P5 derivatives with benzotriazole and residual carboxyl groups separately (Figure 1a), which facilitates the H-bond driven self-assembly [8]. It is well known that APDA moieties could highly react with NO, accompanied by a spontaneous hydrolysis process, resulting in scission of the original chains and a pronounced increase in benzotriazole and carboxyl groups which would form H-bonds [6]. Thus, the final hydrolysis products were first isolated and identified from the M1 solution (chloroform with a trace amount of water and DMSO (v/v = 0.5%/0.5%) at a total concentration of 40 μM) after 24 h treatment with NO. The ^{1}H NMR and ^{13}C NMR spectra are strongly suggestive of the formation of P[5] derivatives with either benzotriazole (M1a) or carboxyl (M1b) terminal groups (Figure 1a; Figures S27, S28, S30, S31). The molecular ion peaks for these two derivates are also found in MS (Figures S29 and S32), which further confirmed the molecular architecture deduced from NMR spectra. Next, studying contributions from the hydrolytic reaction rate is of interest. A kinetics protocol to monitor the hydrolysis process in real time by UV-vis spectrophotometry was conducted to appraise the NO-responsive behavior of M1. As shown in Figures 1b, the M1 exhibits absorptions centered at about 251 and 296 nm. Upon treatment with NO, the absorption bands slowly decrease, and then hypsochromically shift to 246 and 294 nm until the hydrolysis reaction reached a plateau after ~4 h. The absorption intensity changes in 246 and 294 nm of M1 after the reaction with NO was recorded and nonlinear fitting for the absorption intensity change in 294 nm was conducted (Figure 1c), indicating that the designed M1 monomer is highly reactive with NO and capable of gradual hydrolysis on a time scale of hours under ambient conditions. Besides, the slow hydrolysis reaction of M1 was in a quasifirst-order reaction decay model manner with rate constant 9.88×10^{-3} min^{-1}. Subsequently, a similar test to be used for M1 was followed to explore the hydrolysis behavior of PSMs. Thus, a spontaneous hydrolysis of PSMs after NO treatment was evidenced from the change of time-dependent UV-vis spectra. Both the absorption bands centered at 245 and 296 nm for PSMs resulted in slight blue-shift to 243 and 295 nm along with less intensity over time (Figure 1d). Furthermore, the hydrolysis of PSMs after NO treatment was completed almost in 6 h, which is relatively slower than that of M1 monomer.

The attenuation curve of the intensity in 295 nm for PSMs also fitted well with quasifirst-order reaction decay model [9], giving the rate constant of 6.87×10^{-3} min^{-1} (Figure 1e). We presume that a higher steric hindrance environment

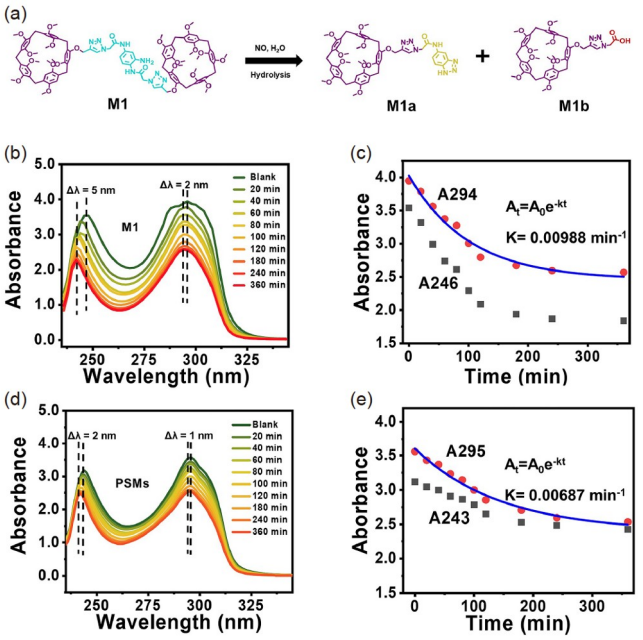

Figure 1 Study of NO-triggered hydrolysis reaction and reaction rate of PSMs. (a) Schematic showing NO induced hydrolysis reaction of M1 to the production of M1a and M1b. (b) Time-dependent absorbance spectra and (c) absorbance intensity changes for M1 (100 μM) treated with 100 μM NO. (d) Time-dependent absorbance spectra and (e) absorbance intensity changes for PSMs (100 μM) treated with 100 μM NO (color online).

existed in PSMs might be attributed to the slower hydrolysis of APDA moieties. Taken together, these results indicate that our designed PSMs can be successfully hydrolyzed in the treatment of NO with the generation of derivatives containing M1a or M1b terminal groups.

While confirmed the slow hydrolysis reaction of PSMs after a NO trigger, it was employed to construct self-assemblies with complex topologies investigated by various microscopies and light scattering technologies. To prepare assembly specimens, a fixed 3:2 complexation stoichiometry of M1 and M2 were first dissolved in chloroform with a trace amount of water and DMSO (v/v = 0.5%/0.5%) at a total concentration of 40 μM. The DMSO is added to increase the water content in chloroform for the hydrolysis reaction. The specimens for microscopies were dropped on silicon wafer or copper grid, followed by rapid lyophilization in liquid nitrogen. The solvent is then removed by sublimation in a dryer to obtain the test samples trapped with preserved aggregate morphologies, and thus the effect of drying on sample preparations can be ruled out. In the absence of NO, TEM and 2D/3D AFM images revealed the formation of spherical morphology of PSMs with average diameter around 40 nm (Figure S26). The solid spherical structure and elemental distribution of PSMs were further confirmed by using dynamic light scattering (DLS, $R_g/R_h = 0.713$, where R_g is the radius of gyration and R_h is the ring height) [10] and HAADF-STEM as well as energy-dispersive X-ray spec-

troscopy (EDS). However, after incubation with NO for 24 h, the spherical PSMs transferred into toroidal structures, as shown in Figure 2a. The zoomed-in TEM images of these STs showed no obvious boundary between the interior and exterior of the toroidal rim, indicating solid structures in the STs (Figure 2a, inset, upright). An AFM profile displayed that the size parameters of a typical ST including peak-to-peak distance R_d, peripheral ring width R_w, and ring height R_h (the detailed definition of R_d, R_w, and R_h can be found in Experimental Procedures Section in the Supporting Information online) are 647, 161, and 24 nm, respectively (Figure 2b, c). It should be noted that the R_w of STs observed by TEM is relatively small compared with the above AFM results, which may be attributed that the unstained and vulnerable organic assemblies are not obvious or partially dissociated by under electron beam [11]. Moreover, either TEM or AFM images for resulted STs show the same contrast between the inner cavity and outer space of the toroids. These results clearly indicate that the formed STs are different from collapsed vesicles, which generally reveal a lighter center and a darker periphery in the AFM or TEM image [12]. The toroid morphology and element composition are also confirmed with HAADF-STEM and EDS spectroscopy (Figure 2d–g), convincingly demonstrating the homogeneous distribution of featured elements C, N and O of M1 and M2 in the STs. Another parameter sensitive to the morphologies of the assemblies is the ratio between radius of hydrodynamic (D_h/2) and radius of gyration (R_g). An average R_g is experimentally determined to be 338 nm by static light scattering (SLS, meanwhile, DLS) testing reveals that these assemblies have an average D_h of 631 nm (Figure 2h) with a polydispersity index (PDI) value of 0.291. Thus, the $R_g/(D_h/2)$ value for the STs in the solution was obtained as 1.07, which compares favorably with the other toroidal system [13]. Another R_g value is also calculated as 330 nm by using a literature reported equation for toroidal assemblies, namely $R_g = 0.5R_d(1+3/4Z^2)^{1/2}$ [14], where $Z = R_d/R_w$ from the typical AFM measurement, R_d = 647 nm, R_w = 161 nm, thus the $R_g/(D_h/2)$ value becomes 1.05. Considering the limitations in the precise measurement of the average size parameters of STs, both the measured and calculated R_g and $R_g/(D_h/2)$ values appear to further support the toroidal morphology existed in the solution. It is noteworthy that the ζ-potential of STs solution is −21.2 mV, which is quite different from that of PSMs (+32.6 mV) (Figure 2i). The negative surface charge is expected to be explained due to the hydrolyzed generation of carboxylic acid groups on the surface of STs. Additionally, the toroids could be prepared only not on carbon-supported copper grids (Figure 2a) and silicon wafer (Figure 2b), but also on the mica substrate (Figure S33a, b) and highly oriented pyrolytic graphite (HOPG) substrate (Figure S33c, d). Concerning the surface properties differences among these substrates, it is unlikely to be the "coffee stain" drying effects since the contact line pinning and contact angle hysteresis, which plays a critical role in the formation of coffee-ring effect, will be significantly changed by replacing substrates with various surface characters [15]. Especially, the as-prepared toroids are not round enough on HOPG surface, which should be attributed that they are assembled from soft molecules.

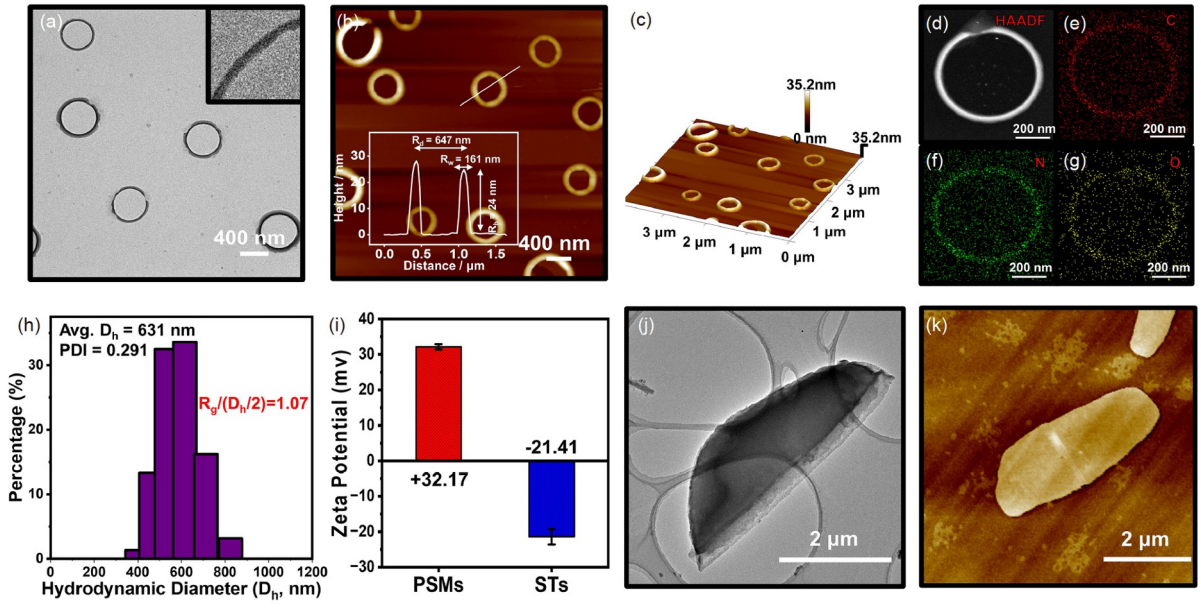

Figure 2 Formation of STs and control sample NSs after reaction with NO. (a) TEM mages of STs (inset: magnified morphologies of STs). (b) AFM images of STs (the inset is the typical size parameter profile for STs). (c) AFM 3D images of STs. (d–g) HAADF-STEM image and EDS mapping. C: red, N: green, O: yellow. Preparation solvent is chloroform solution containing trace water and DMSO (v/v = 0.5%/0.5%). (h) DLS analysis of STs. (i) Zeta potentials of PSMs and STs. (j, k) AFM and TEM images of representative structure of NSs formed in NO-induced rapid hydrolysis process (color online).

As a comparison, another self-assembly process under NO-induced rapid hydrolysis was necessary to implement. Since it was difficult to realize fast hydrolysis without significantly changes in both the initial state and terminal state of this assembly system, fast mixing the fully hydrolyzed M1a, M1b, and M2 molecules with the mole ratio of 3:3:2 was adopted to simulate the fast hydrolysis process of PSMs after reaction with NO. This particular sample was then examined by AFM and TEM (Figure 2j, k), revealing the distinct 2D NSs rather than those of STs obtained by NO-induced slow hydrolysis. On the other aspect, when the prepared STs solution was heated up to 55 °C for 24 h to accelerate denaturation and cooled slowly (1 K min^{-1}), the AFM and TEM images (Figures S34 and S35) exhibited a similar morphology to those assemblies under NO-induced rapid hydrolysis instead of the STs. This intriguing phenomenon suggests that the ST is a kinetically controlled product (most probably the kinetically trapped species, in view of its stability in r.t.) [16], whereas the thermodynamically controlled product is 2D NSs formed during a fast hydrolysis process (Scheme 1).

3.2 Visualization of topological evolution process of STs

The visualization of topological evolution process makes great efforts to the exploration of mechanistic details of hierarchical organization of self-assembled structures [17]. Here, intermediate structures of STs were successfully captured by AFM and TEM, and the time-dependent toroid formation was carefully investigated by statistical analysis. We collected self-assembled intermediate solutions at time intervals after adding excess NO into the PSMs solution. The intermediates were also dropped on silicon wafer or copper grid, followed by rapid lyophilization in liquid nitrogen. Then the solvent is removed by sublimation in a dryer to obtain the test samples trapped with preserved aggregate morphologies and the effect of drying on sample preparations can be ruled out. These morphologies transformation from PSMs to STs is a time-dependent evolution process as illustrated in Figure 3. The morphologies of intermediates were observed distinctly by AFM as shown in Figure 3a1–a6. At early stage of 5 min after the addition of NO, larger PSMs were observed in the reaction mixture with an average diameter of 90 nm (Figure 3a1, b1) compared with the PSMs without the addition of NO (Figure S26). Further prolonging the reaction to 30 min, larger PSMs started to deform anisotropically (Figure 3a2, b2). And then, these deformed PSMs kept growing in the longitudinal directions by integrating with each other after 1 h, leading to the formation of WMs curved with certain bending degree (Figure 3a3, 3b3). It should be pointed out that a certain amount of deformed PSMs were still maintained because of the

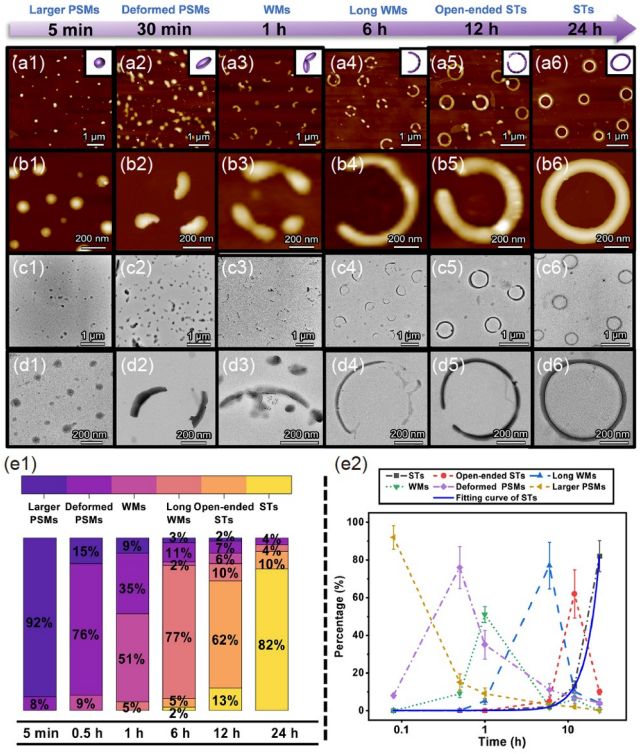

Figure 3 Visually morphological evolution with time-dependent feature during the formation of STs after the treatment of NO at varied time. From left to right: column 1, larger PSMs (5 min); column 2, deformed PSMs (30 min); column 3, WMs (1 h); column 4, long WMs with curvature (6 h); column 5, open-ended STs (12 h); column 6, STs (24 h). (a) AFM images of the intermediate assemblies and final STs obtained. Insets are the representative models in each stage. (b) Enlarged AFM images of representative assemblies at varied time. (c) TEM images of the intermediate assemblies and final STs obtained. (d) Enlarged TEM images of representative assemblies at varied time. (e1) Distribution frequency N of larger PSMs (violet bars), deformed PSMs (purple bars), WMs (purplish red bars), long WMs (rose bars), open-ended STs (orange bars) and intact STs (yellow bars) along the morphological evolution at given reaction time. (e2) Time dependence of corresponding N as determined by AFM (color online).

insufficient NO-induced hydrolysis morphology transformation, which may be considered as a nonuniform transformation that continuously evolves and depends upon reaction time [18]. After reaction for 6 h, WMs could not be found in the AFM microscope field while the connection junctions in long WMs were clearly visible (Figure 3a4, 3b4). After a longer elongation period, massive open-ended STs appeared after 12 h (Figure 3a5, 3b5). Finally, many intact STs with relative unity were observed after approximately 24 h (Figure 3a6, 3b6). Further, measured width of individual ST rim was about 150 nm, which was comparable to the cross-section distance of initial deformed PSMs (Figure 3a2), indicating that the STs was indeed formed by the coalescence of single deformed PSM. Besides, TEM images of the typical intermediate morphologies during the formation of the toroid aggregates were also provided in Figure 3c, d, which agreed well with those from AFM observations. In addition, AFM image (Figure 3b5) revealed a

few rough and imperfect surface with ring-junction points, which may reflect the hierarchical self-assembly process of PSMs in the presence of NO [19].

To gain a better understanding of the formation kinetic of STs, the distribution frequencies of larger PSMs (violet bars), deformed PSMs (purple bars), WMs (purplish red bars), long WMs (rose bars), open-ended STs (orange bars) and intact STs (yellow bars) along the morphological evolution at given reaction time were estimated (Figure 3e1). The distribution frequency N is defined as the ratio of various morphologies by measuring a fixed field of view of AFM (1 mm^2) and plotted as the function of hydrolysis time [20]. Overall, the PSMs gradually fuse to STs *via* a series of intermediates with long time scales of hours. In the first half-hour, most of the assemblies in the field of view of AFM were PSMs or WMs while the STs were hardly observed. After incubation for 1 h, most of PSMs were transferred while the proportion of WMs reached up to 51%. With the extension of time, a further topological revolution occurred and 77% long WMs appeared within 6 h. Subsequently, the proportion of long WMs started to drop while the ones of open-ended and intact STs increased. Much higher proportions (82%) of intact STs were formed after 24 h incubation while the WMs and open-ended STs were almost absent. Furthermore, nonlinear fitting for analysis of time-dependent changes in the fractions of intact STs were also inferred, in which the growth of STs fits the power function model allometric1 well (adjusted $R^2 = 0.999$) (Figure 3e2). All these findings indicated that the STs were formed in a manner through coalescence-elongation-closure process initially from PSMs building blocks. Additionally, we also extended the sampling time of the STs up to 3 d at room temperature to test kinetic stability. The results showed negligible morphology change for STs (Figure S36), indicating that these assembled structures can be trapped solidly in the state probably by virtue of its closed topology [16,21].

3.3 Regulation of geometrical parameters of STs

The initial concentration of the monomers is one of the vital factors to the regulation of assembly pathways. Thus, this enlightens us to wonder whether the concentration of monomer might act as a regulatory factor in finely manipulating the geometry parameters of STs in this system. Firstly, the critical aggregation concentration (CAC) of STs from M1 and M2 in a ratio of 3:2 was verified with the value of 1.32 μg mL^{-1} by the pyrene probe method (Figure S37) [22]. On the other hand, STs began to disassociate into small irregular aggregates at higher concentration (100 μM) (Figure S38). In this scenario, we decided to study the changes of geometrical parameters of STs at monomer concentrations within the range from 30 to 70 μM, in which the STs are well formed after reaction with NO for 24 h. The featured geometrical parameters of STs are captured by AFM, 500 STs at each concentration were measured by hand using the software ImageJ (National Institutes of Health, USA). Surprisingly, we discovered that the geometrical parameters of STs including R_d, R_w, and R_h gradually increased with an increasing of the initial monomer concentration (Figure 4a–e). At a lower concentration of 30 μM, STs with average size

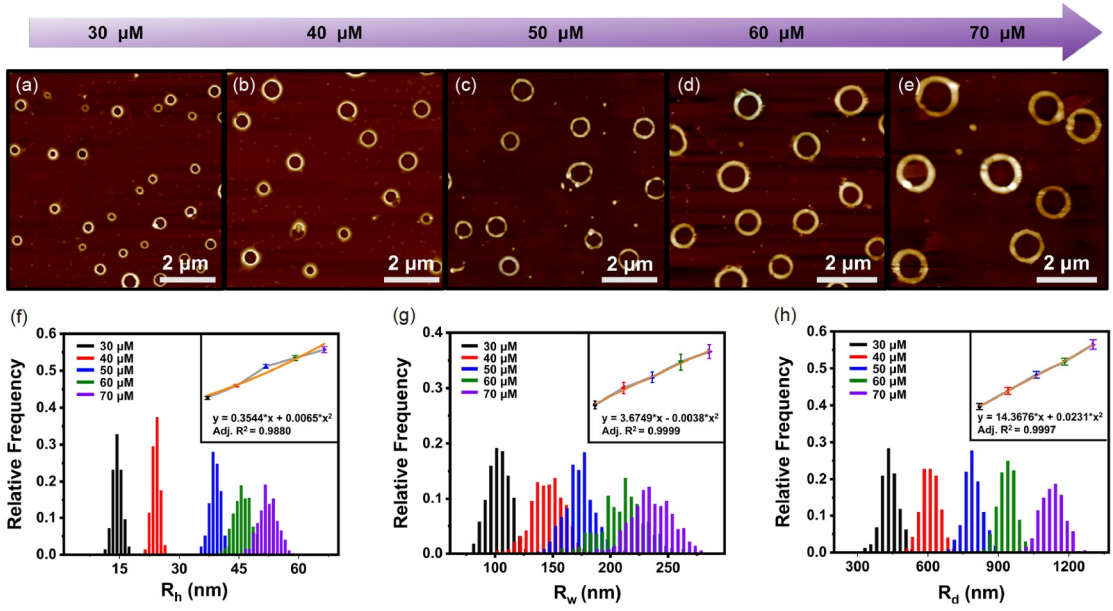

Figure 4 Regular modulation of geometry parameters R_h, R_w, and R_d of STs in concentration-dependent manner. (a–e) The AFM images showing the typical size change of STs according to the increase of concentration of M1 and M2. (a) 30 μM; (b) 40 μM; (c) 50 μM; (d) 60 μM; (e) 70 μM. Relative frequency profiles of the (f) R_h, (g) R_w, and (h) R_d as measured by AFM and imageJ software across the STs, corresponding to different concentrations of 30 μM (black), 40 μM (red), 50 μM (blue), 60 μM (green), and 70 μM (purple). Insets are the statistical average sizes of R_h, R_w, and R_d as a function of the assembly concentrations (color online).

parameters, R_h = 14.6 nm, R_w = 104.5 nm, and R_d = 443.8 nm were obtained (Figure 4a). In contrast, at a concentration of 70 μM, the average R_h, R_w, and R_d values of STs further increased to 52.3, 236.3, and 1,122.3 nm (Figure 4e). Apparently, all three geometrical parameters are near-gaussian distribution in each group, and they have significantly positive relationships with the assembly concentration. Then, mathematical statistics proved that the principle of polynomial curve fitted the relationship well between average geometrical parameter changes and initial concentration (Figure 4f–h), indicating that modulate the parameters of STs with ease. When comparing Figure S26 (40 μM) with Figure S39 (70 μM), the PSMs diameter increased from ~45 to ~100 nm as determined by AFM, indicating that the assemblies prefer to adopt a larger size to favor a lower degree of interfacial curvature and energy. This phenomenon is reported in certain self-assemble system as well. For instance, as the concentration increases in block copolymer system, the system free energy elevates due to the intensive copolymer-solvent interaction. Then, the local packing changes to minimize the free energy, leading to a decrease of the local curvature [23]. Thus, the formation of different nanostructures [24] and subtle size change of assemblies [25] could be obtained in a concentration-dependent way. Therefore, the geometrical parameters of STs can be regularly modulated in a simple concentration-dependent manner.

3.4 Validation of the role of H-bonds in driving the formation of STs

The remaining issue of importance is the driving forces involved in the formation process. Since NO-triggered hydrolysis products M1a or M1b groups (Figure 1a) usually plays important role in both of H-bonds donor and acceptors, we then sought to investigate the presence of H-bonds in STs by variable temperature ^{1}H NMR experiments. As the solution of STs was heated up to 50 °C, the amide proton peak at 9.91 ppm broadened and upfield-shifted to 9.46 ppm (Figure 5a). This reveals the enhanced shielding and exchange abilities of the amide proton at an elevated temperature, which is attributed to the disruption of intermolecular H-bonds involving amide group in resulted M1a motif. Unfortunately, even at high temperatures, the protons of the carboxyl group and triazole were not visible, owing to the quick exchange and strong H-bond interactions of these groups in chloroform. Alternatively, from variable-temperature Fourier transform infrared (FTIR) spectra (Figure 5b), red-shift of the peak assigned to O–H stretching vibration of carboxyl appeared at 2,919 cm^{-1} after the hydrolysis process, suggesting intermolecular H-bonds involving carboxyl groups in the aggregated state [26]. Moreover, the C=O stretching band enhanced and red-shifted to

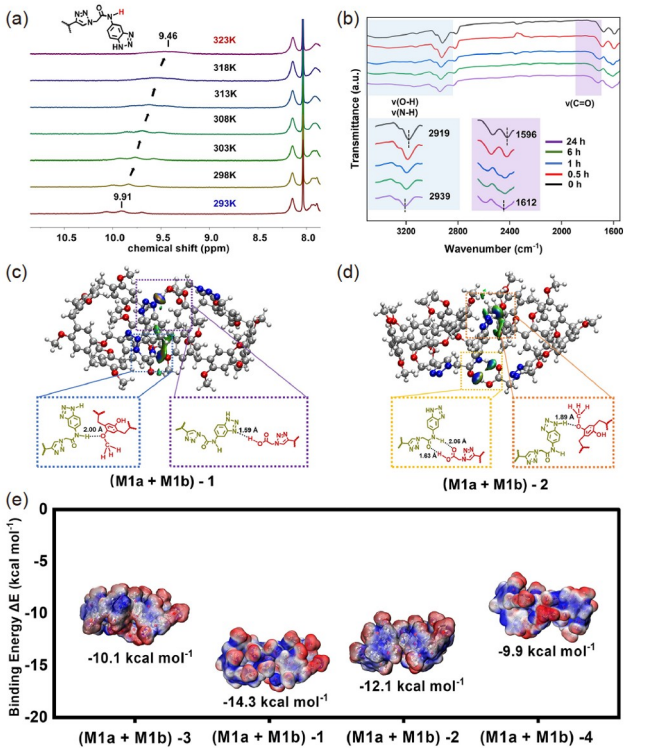

Figure 5 Validation of the role of H-bonds in driving the formation of STs. (a) Variable-temperature ^{1}H NMR of STs in $CHCl_3$ (293–323 K). The amide proton peak at 9.91 ppm broadened and upfield-shifted at an elevated temperaure. (b) Variable-temperature FT-IR studies showing characteristic O–H and C=O stretching vibration of carboxyl at 298 K. (c, d) IGM analysis of favorable H-bonds interaction mode named (M1a+M1b)-1 and (M1a+M1b)-2 between M1a and M1b. The grids show the enlarged H-bond sites. (e) Calculated binding energies of four possible H-bonds interaction models (color online).

1,596 cm^{-1}, corresponding to typical values of H-bonds of the carbonyl group [27]. These findings demonstrate the existence of multiple intermolecular H-bonds between M1a and M1b molecules during the morphology transition process. The geometry optimization of intermolecular H-bonds between hydrolysis products M1a and M1b was further performed with the semi-empirical xtb program, owing to the very large (~250 atoms) model. The independent gradient model (IGM) analysis and electrostatic potential mapped molecular surface (ESP) were performed with the Multiwfn program2 to give direct visualization of the real space interactions. As shown in Figure 5c, d, two favorable H-bond interaction models were named (M1a+M1b)-1 and (M1a +M1b)-2 between M1a and M1b, respectively. Specifically, (M1a+M1b)-1 model contains two intermolecular H-bonds such as the amide N–H group of M1a as donor and C–O group of M1b as acceptor, and carboxyl O–H group of M1b as donor and triazole ring N atom of M1a as acceptor. While N–H···O and O–H···O H-bonds between amide group of M1a and carboxyl group of M1b were depicted in (M1a +M1b)-2 model as well. The binding energies of (M1a +M1b)-1 and (M1a+M1b)-2 which had lower energies

among four possible binding models, were also calculated as −14.3 and −12.1 kcal mol^{-1}, respectively (Figure 5e). Taken together with studies of NMR and FTIR, these observations supported that the H-bonds generated from the NO-induced hydrolysis process are the predominated driven forces to the formation of STs.

3.5 Proposed mechanism for self-assembly process from PSMs to STs

Integrating the aforementioned characterization data during the assembly process, we attempted to infer the underlying formation mechanism of STs. Overall, at the first stage (PSMs to WMs), these newly formed complexes or oligomers by host- guest interactions among M2, hydrolyzed M1a, M1b, and unhydrolyzed M1 tend to form relatively disordered prenuclear clusters (Figure 6a1, a2). Thus the expulsion of solvent from assemblies was enhanced, leading to the increase of conformational degrees of system which could be a prominent driven force to promote the fusion and elongation of deformed PSMs to the formation of WMs in an enthalpy-driven way (Figure 6a3). At the second stage, the morphology and two H-bond-rich terminals of formed longer WMs, contribute to the improvement of interfacial energy between WMs surface and solvent molecules. As a consequence, to lower the interfacial energy, the WMs could come over their intrinsic bending energy, resulting in the formation of curvature morphology (Figure 6a3, a4). Notably, the two terminals of one open-ended STs had a tendency to joint together if the length of WM is appropriate, since the unique end-cap energy resulted from wormlike morphology with high length–diameter ratio (Figure 6a5). For a detailed discussion and relevant structural control experiments, please refer to section 8 of the Supporting In-

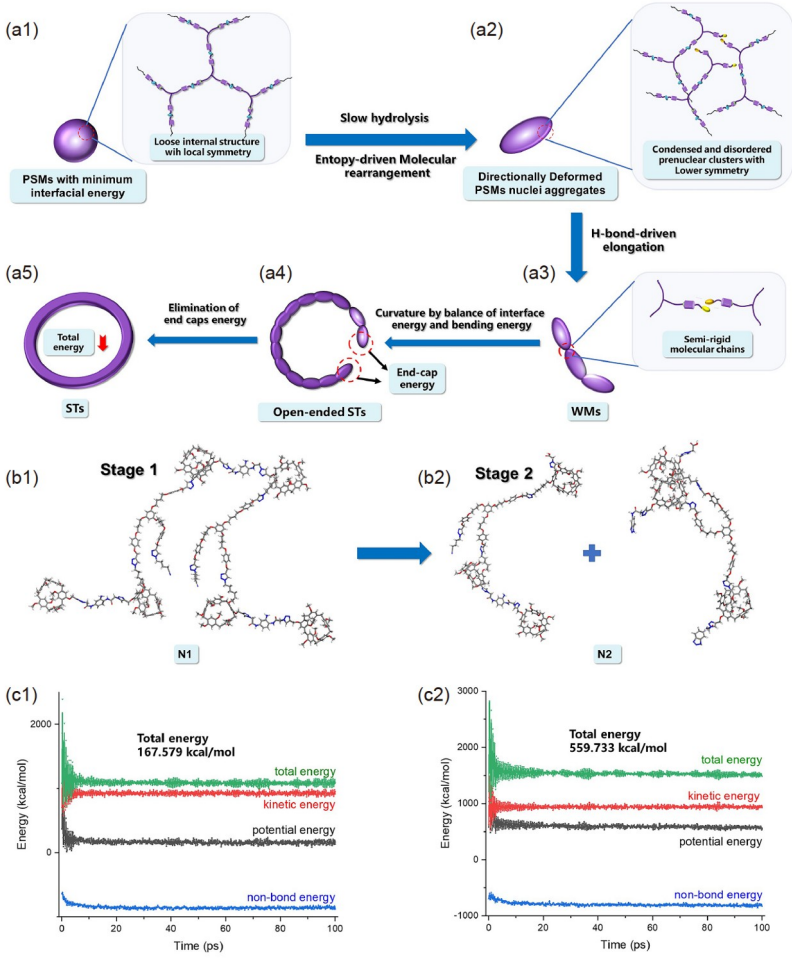

Figure 6 Proposed mechanism for self-assembly process from PSMs to STs under NO-triggered hydrolysis. (a1) Initial spherical PSMs with minimum interfacial energy consist of loose SPs with local symmetry. (a2) The slow hydrolysis induced the formation of disordered prenuclear clusters and further nucleation by entropy, and thus the PSMs deformed and fused into anisotropic WMs. (a3) The newly formed H-bonds in this system could be a prominent driven force to promote the fusion and elongation of deformed PSMs to the formation of WMs. (a4) The WMs trended to bend by the balance of their intrinsic bending energy and interfacial energy. (a5) The intact STs were emerged driven by the unique end-cap energy resulted from wormlike morphology with high length-diameter ratio. (b) Molecular structures of two model host-guest complexes named N1 and N2 which represented molecules in PSMs with different hydrolysis stages. (c) Energy evolution curves of N1 and N2, respectively (color online).

formation online. Besides, the WAXS results indicate that the evolution from WMs to STs is accompanied by enhanced rigid due to closer molecular arrangements. The appropriate assemblies chains rigidity induced by this hydrolysis reaction may also be a significant factor in the formation of STs [21,28]. On top of that, the conformation optimization of the energy evolution of the system during the self-assembly process was monitored by MD simulation refer to previous study [29]. To simplify the computational process, a MD simulation was performed by constructing a crystalline cell composed of a series of model host-guest complexes named N1 and N2 (Figure 6b), which represented molecules in PSMs with different hydrolysis stages. This higher energy state indicated that the system reached an unstable thermodynamic state after hydrolysis, so it supports the assembly process containing the enthalpy driven processes. Moreover, the kinetic energy, which is related to the entropy, is growing over trend (Figure 6c). This may imply that the hydrolysis reaction promotes an increase in entropy as well. Therefore, these simulation results correlate well with the experimental observations, supporting the proposed self-assembly mechanism induced by NO-triggered slow hydrolysis.

4 Conclusions

In summary, we explored a NO-triggered slow hydrolysis strategy of accessing STs straightforwardly, thus enhancing the control over STs by hydrolysis to retard the rate of self-assembly and modulate the kinetic pathway. The self-assembly process of STs is accomplished in the manner of long time-scale evolution, thus providing visualized intermediates in their formation procedures. The geometry parameters including height, width, and diameter of the toroids can be regularly modulated by simply adjusting the concentration of the initial monomers as well. The mechanism analysis shows that the kinetically trapped STs are formed by two sequential steps involving nucleation-growth and fusion-curvature-closure processes. The slow hydrolysis acts as a fundamental factor throughout the self-assembly process of STs, not only leading to the disordered entropy-driven nucleation, H-bond-driven growth and fusion, but also contributing to a semi-rigid structure to subtle and synergistic balance between the interfacial energy and bending energy for the curvature and closure to form the final STs. We anticipate that the NO-triggered slow hydrolysis strategy developed in this work sheds light on the generic nature of a chemical reaction-driven approach for the controlled construction of the biomimetic self-assemblies with complex topological structures by using synthetic building blocks.

Acknowledgements This work was supported by the National Science Foundation of China (22071197, 22022107, 82304889). The authors thank the Analytical & Testing Center of Northwestern Polytechnical University for electron microscope tests.

Conflict of interest The authors declare no conflict of interest.

Supporting information The supporting information is available online at chem.scichina.com and link.springer.com/journal/11426. The supporting materials are published as submitted, without typesetting or editing. The responsibility for scientific accuracy and content remains entirely with the authors.

1 (a) He H, Guo J, Lin X, Xu B. *Angew Chem Int Ed*, 2020, 59: 9330–9334; (b) Feng Z, Wang H, Xu B. *J Am Chem Soc*, 2018, 140: 16433–16437
2 (a) Sun Z, Kim JH, Zhao Y, Bijarbooneh F, Malgras V, Lee Y, Kang YM, Dou SX. *J Am Chem Soc*, 2011, 133: 19314–19317; (b) Wan Y, Zhao Y. *Chem Rev*, 2007, 107: 2821–2860; (c) Jiang Z, Xu X, Ma Y, Cho HS, Ding D, Wang C, Wu J, Oleynikov P, Jia M, Cheng J, Zhou Y, Terasaki O, Peng T, Zan L, Deng H. *Nature*, 2020, 586: 549–554
3 (a) Weißenfels M, Gemen J, Klajn R. *Chem*, 2021, 7: 23–37; (b) Tena-Solsona M, Rieß B, Grötsch RK, Löhrer FC, Wanzke C, Käsdorf B, Bausch AR, Müller-Buschbaum P, Lieleg O, Boekhoven J. *Nat Commun*, 2017, 8: 15895; (c) Heuser T, Steppert AK, Molano Lopez C, Zhu B, Walther A. *Nano Lett*, 2015, 15: 2213–2219; (d) Boekhoven J, Brizard A , Kowlgi K , Koper G , Eelkema R, van Esch J . *Angew Chem Int Ed*, 2010, 49: 4825–4828
4 (a) Chen W, Chen Z, Chi Y, Tian W. *J Am Chem Soc*, 2023, 145: 19746–19758; (b) Gao Z, Shi L, Yan F, Han Y, Yuan W, Tian W. *Angew Chem Int Ed*, 2023, 62: e202302274; (c) Xiao X, Chen H, Dong X, Ren D, Deng Q, Wang D, Tian W. *Angew Chem Int Ed*, 2020, 59: 9534–9541; (d) Huo H, Xiao X, Chang L, Xiong X, Shi M, Wang J, Tian W. *Sci China Chem*, 2023, 66: 2070–2082
5 (a) Liu C, Li M, Sun J, Li P, Bai Y, Zhang JA, Qian Y, Shi M, He J, Huo H, Pang J, Fan L, Tian W. *Adv Funct Mater*, 2022, 32: 2205043; (b) Bai Y, Shang Q, Wu J, Zhang H, Liu C, Liu K. *ACS Appl Mater Interfaces*, 2022, 14: 37424–37435
6 (a) Hu J, Whittaker MR, Duong H, Li Y, Boyer C, Davis TP. *Angew Chem Int Ed*, 2014, 53: 7779–7784; (b) Hu J, Whittaker MR, Yu SH, Quinn JF, Davis TP. *Macromolecules*, 2015, 48: 3817–3824
7 Chen W, Li X, Liu C, He J, Qi M, Sun Y, Shi B, Sepehrpour H, Li H, Tian W, Stang PJ. *Proc Natl Acad Sci USA*, 2020, 117: 30942–30948
8 Thirunavukkarsu A, Sujatha T, Umarani PR, Nizam Mohideen M, Silambarasan A, Kumar RM. *J Cryst Growth*, 2017, 460: 42–47
9 Geng WC, Jia S, Zheng Z, Li Z, Ding D, Guo DS. *Angew Chem Int Ed*, 2019, 58: 2377–2381
10 Wu C, Zhou S. *Macromolecules*, 1995, 28: 8381–8387
11 (a) Lamvik MK. *J Microsc*, 1991, 161: 171–181; (b) Egerton RF. *Ultramicroscopy*, 2013, 127: 100–108
12 Zhang L, Eisenberg A. *Science*, 1995, 268: 1728–1731
13 Presa-Soto D, Carriedo GA, de la Campa R, Presa Soto A. *Angew Chem Int Ed*, 2016, 55: 10102–10107
14 Huang H, Chung B, Jung J, Park HW, Chang T. *Angew Chem Int Ed*, 2009, 48: 4594–4597
15 Mampallil D, Eral HB. *Adv Colloid Interface Sci*, 2018, 252: 38–54
16 Adhikari B, Aratsu K, Davis J, Yagai S. *Angew Chem Int Ed*, 2019, 58: 3764–3768
17 Yang Y, Wang Y, Zhao L, Liu Y, Ran F. *Adv Energy Mater*, 2022, 12: 2103158
18 Xu B, Qian H, Lin S. *ACS Macro Lett*, 2020, 9: 404–409
19 Li D, Jia X, Cao X, Xu T, Li H, Qian H, Wu L. *Macromolecules*, 2015, 48: 4104–4114
20 Qiu H, Oliver AM, Gwyther J, Cai J, Harniman RL, Hayward DW, Manners I. *Macromolecules*, 2019, 52: 113–120
21 Gao L, Hu R, Xu P, Lin J, Zhang L, Wang L. *Nanoscale*, 2020, 12: 296–305
22 Yu G, Yu W, Shao L, Zhang Z, Chi X, Mao Z, Gao C, Huang F. *Adv*

Funct Mater, 2016, 26: 8999–9008
23 (a) Guo C, Luo Y, Zhou R, Wei G. *ACS Nano*, 2012, 6: 3907–3918; (b) Smart T, Lomas H, Massignani M, Flores-Merino MV, Perez LR, Battaglia G. *Nano Today*, 2008, 3: 38–46
24 Kim J, Han TH, Kim YI, Park JS, Choi J, Churchill DG, Kim SO, Ihee H. *Adv Mater*, 2010, 22: 583–587
25 Kim D, Kim E, Lee J, Hong S, Sung W, Lim N, Park CG, Kim K. *J Am Chem Soc*, 2010, 132: 9908–9919
26 Ogi S, Sugiyasu K, Manna S, Samitsu S, Takeuchi M. *Nat Chem*, 2014, 6: 188–195
27 Serrano Ruiz D, Alonso Cristobal P, Laurenti M, Rubio Retama J, Lopez-Cabarcos E. *J Phys-Conf Ser*, 2014, 549: 012012
28 Ni B, Huang M, Chen Z, Chen Y, Hsu CH, Li Y, Pochan D, Zhang WB, Cheng SZD, Dong XH. *J Am Chem Soc*, 2015, 137: 1392–1395
29 Sun H, Chen S, Li X, Leng Y, Zhou X, Du J. *Nat Commun*, 2022, 13: 2170